Additive manufacturing of anti-SARS-CoV-2 Copper-Tungsten-Silver alloy

John Robinson[1,2], Arun Arjunan[1*], Ahmad Baroutaji[1], Miguel Martí[3], Alberto Tuñón-Molina[3], Ángel Serrano-Aroca[3] and Andrew Pollard[1]

[1]Additive Manufacturing of Functional Materials (AMFM) Research Group, Centre for Engineering Research and Innovation (CEIR), University of Wolverhampton, Telford Innovation Campus, Telford TF2 9NT, UK

[2]Additive Analytics Ltd., Stirchley Road, Telford TF3 1EB, UK

[3]Biomaterials and Bioengineering Lab, Centro de Investigación Traslacional San Alberto Magno, Universidad Católica de Valencia San Vicente Mártir, c/Guillem de Castro 94, 46001 Valencia, Spain.

Abstract

Purpose – The COVID-19 pandemic emphasises the need for antiviral materials that can reduce airborne and surface-based virus transmission. The study proposes the use of additive manufacturing (AM) and surrogate modelling for the rapid development and deployment of novel copper-tungsten-silver (Cu-W-Ag) microporous architecture that shows strong antiviral behaviour against SARS-CoV-2.

Design/methodology/approach – The research combines Selective Laser Melting (SLM), in-situ alloying and surrogate modelling to conceive the antiviral Cu-W-Ag architecture. The approach is shown to be suitable for redistributed manufacturing by representing the pore morphology through a surrogate model that parametrically manipulates the SLM process parameters: hatch distance (h_d), scan speed (S_s) and laser power (L_p). The method drastically simplifies the 3D printing of microporous materials by requiring only global geometrical dimensions solving current bottlenecks associated with high CAD data transfer required for the AM of porous materials.

Findings – The surrogate model developed in this study achieved an optimum parametric combination that resulted in microporous Cu-W-Ag with average pore sizes of 80 µm. Subsequent antiviral evaluation of the optimum architecture showed 100% viral inactivation within 5 hours against a biosafe enveloped RNA viral model of SARS-CoV-2.

* Corresponding author. Address: School of Engineering, Faculty of Science and Engineering University of Wolverhampton, Telford Innovation Campus, Telford, TF2 9NT, UK
Tel.: +44 1902 323829; fax: +44 01902 323843
E-mail address: a.arjunan@wlv.ac.uk (Dr. Arun Arjunan)

Research limitations/implications – The Cu-W-Ag architecture is suitable for redistributed manufacturing and can help reduce surface contamination of SARS-CoV-2. Nevertheless, further optimisation may improve the virus inactivation time.

Practical implications – The study was extended to demonstrate an open-source 3D printed Cu-W-Ag antiviral mask filter prototype.

Social implications – The evolving nature of the COVID-19 pandemic brings new and unpredictable challenges where redistributed manufacturing of 3D printed antiviral materials can achieve rapid solutions.

Originality/value – The papers present for the first time a methodology to digitally conceive and print-on-demand a novel Cu-W-Ag alloy that shows high antiviral behaviour against SARS-CoV-2.

Keywords: SARS-CoV-2; COVID-19; Silver; Copper; Tungsten; Additive manufacturing; 3D Printing; antiviral; Selective Laser Melting.

1. Introduction

March 11th, 2020, saw the World Health Organisation (WHO) declare a global pandemic following the COVID-19 outbreak. The prolonged outbreak combined with concerns regarding second, and third waves (at time of writing) of reinfection resulted in industry and academic institutions combining their resources and multidisciplinary knowledge to develop products that can reduce virus transmission [1–3]. Although most infections result in mild symptoms, severe cases have been reported for all ages [4,5] with health care workers at increased risk [1,6,7]. Despite significant research efforts, effective preventions techniques have not materialised [8] and the long-term effects of COVID-19 are yet to be evaluated. Numerous virus mutations are also emerging that may possess vaccine evasiveness being a concern further emphasising the requirement for enhanced transmission control and prevention. A model used to assess the effectiveness of isolation and contact tracing on virus transmission concluded isolation and near-perfect contact tracing are insufficient for various plausible outbreak scenarios [9]. Since asymptomatic virus infection is common [10], preventative transmission measures are essential. As such virus transmission can be direct (human-to-human) or indirect (airborne and/or contaminated surfaces) including respiratory droplets through talking, singing, coughing, and sneezing [5].

Currently, common surface contamination prevention measures include increased disinfection, hand washing, sanitising, and the use of disposable gloves. Face coverings have also become

mandatory in many community settings due to the airborne nature of the virus and are seen as an essential COVID-19 suppression measure [3]. Face coverings/masks are generally produced as single-use items due to contamination risk, however, this raises issues related to appropriate use, disposal, and associated environmental effects [11]. The careless disposal of contaminated masks leads to other modes of transmission. Consequently, the requirement for long life masks and mask filters that can be disinfected is essential [5].

The COVID-19 pandemic has led to supply chain and manufacturing limitations causing shortages of essential COVID-19 related supplies including Personal Protective Equipment (PPE), nasopharyngeal swabs, and ventilators [2,3,12] highlighting the requirement for on-demand and redistributed manufacturing. Surfaces can sustain infectious viruses from a few hours to nine days depending on the surface material and morphology [3]. For example, stainless steel that is widely found in hospitals and medical settings can sustain SARS-CoV-2 survival for up to 7 days [13]. Accordingly, chemists, metallurgists, and materials specialists have been investigating numerous potential solutions to limit virus spread [7,14,15]. Emerging drug and antibiotic resistance in addition to viral mutations have called for alternative antimicrobial resistant materials and therapies, where novel material compositions and antimicrobial surfaces offer significant potential [16–20].

Antimicrobial biomaterials in literature include metals (Ag, Zn, Cu, Zr) [21–24], non-metals (Se, hydrogels) [25] and organic substances (antibiotics, antibacterial peptides, chitosan) [14,26–30]. Silver (Ag) offers wide spectrum antibacterial, [31] antifungal, and antiviral properties against SARS-CoV-2 due to its ions (Ag+) interfering with virus RNA/DNA [17,30,32]. Ag+ ions can supply long-duration antiviral properties making them suitable for Class I devices [33] such as wound dressings, pin site infections, face visors, and masks amongst others. However, the relatively high-cost offers challenges for large-scale implementation and scale-up in its pure form [30].

By similar mechanisms copper (Cu) and its ions (Cu+) have been highlighted with anti-SARS-CoV-2 properties with the advantage of having a relatively lower cost [11,34]. Hutasoit *et al.* [34] used the cold spray Additive Manufacturing (AM) technique to develop Cu coating on stainless steel touch surfaces showing a 99.2% virus inactivation after 5 hours [34]. A recent review by Cortes *et al.* [14] also demonstrates the potential for Cu nano-compounds for anti-SARS-CoV-2 filters, face masks, clothing, and surfaces stating significant SARS-CoV-2 inactivation in four hours [14]. A recent trial by Purdue University [11] embedded Cu nanoparticles within mask fibres for potential antiviral benefits. Cu have also demonstrated antimicrobial activity against *Micrococcus luteus*, *S. aureus*, *E. coli*, *K. pneumoniae* and *P. aeruginosa* in addition to Methicillin-resistant *Staphylococcus aureus* (MRSA) [35]. Makvandi *et al.* [36] suggests that the antibacterial efficacy of Cu against certain microbes are comparable to antibiotics.

Although limited, emerging research has shown tungsten (W) to offer antimicrobial effects against common pathogens such as Gram-negative *Escherichia coli* and Gram positive *Staphylococcus aureus* [37,38]. Matharu *et al.* [38] and Syed *et al.* [37] demonstrated the potency of tungsten oxide and tungsten nanoparticles as having antimicrobial activities respectively. Furthermore, studies have shown coronaviruses to be temperature sensitive and therefore indirect metallic antiviral properties that include surface redox reactions, free radicals, and localised heat generation through exciton also interfere with virus replication and adhesion [30].

Therefore, the use of metals such as Cu, Ag, and W show promising potential for antimicrobial applications due to their broad-spectrum antimicrobial properties combined with ion release and redox reactions [14,31,34,37]. This makes them worthy candidates to be explored for the fabrication of on-demand antimicrobial biomaterials. Although the antimicrobial benefits of Ag, Cu, and W are being reported [14,17,31,39–42], the antiviral performance of these materials as a potential 3D printed biomaterial in relation to SARS-CoV-2 is yet to be established. As such the work reported here is the first to demonstrate both the 3D printing and antiviral evaluation of a Cu-W-Ag biomaterial suitable for redistributed manufacturing.

Redistributed Manufacturing transforms how emergency medicine and devices are developed by offering mass personalisation close to point-of-care [43–46]. It has the potential to make the overall system resilient against supply chain disruption, reduce waste, and ensure preparation for situations where supply chain disruptions are likely (such as the COVID-19 crisis). Additive Manufacturing (AM) (also known as 3D printing) is widely considered as the enabling technology that offers the highest potential for the rapid development and deployment of medical devices alleviating supply chain constraints [47–51]. However, achieving this require the development of functional biomaterials that can be additively manufactured without complex pre-processing [52–54]. This research combines application-specific antiviral Cu-W-Ag feedstock and 3D printed in-situ alloying to digitally fabricate on demand antiviral mask filters satisfying the redistributed manufacturing criteria.

A proof-of-concept redistributed manufacturing methodology which further simplifies the printing process by removing Computed Aided Design (CAD) porous data and replacing them with direct 3D printing Selective Laser Melting (SLM) process parameters to inform the resultant pore geometries. Recent antiviral studies demonstrate phage phi 6 as a suitable biosafe RNA viral model of SARS-CoV-2 due to the shortage of biosafety level 3 laboratories [55]. Phi 6 is a double-stranded RNA virus with three-part, segmented, totalling ~13.5kb in length. Even though this type of lytic bacteriophage belongs to the Group III of the Baltimore classification [56], it has a lipid membrane around their nucleocapsid as SARS-CoV-2. Therefore, the resultant 3D printed structures are exposed to this biosafe viral model of SARS-CoV-2 to assess the anti-SARS-CoV-2 potential of the Cu-W-Ag material.

While the methodology reported here informs prototype face mask filter geometries, the approach can be adopted for developing complex Heating, Ventilation, and Air Conditioning (HVAC) antiviral filtration systems for both the general community and health care settings alike. The approach presented in this paper circumvents the need for large and complex CAD files to inform porosity data. Instead, the pore architecture is conceived through SLM process parameters that allows for the fabrication of on-demand anti-SARS-CoV-2 filters with minimal pre-processing. The method alleviates the need for high-performance workstations often required for complex CAD geometry preparation. As such, this research is the first open and collaborative approach in the digitalised manufacture of an anti-SARS-CoV-2 material.

2. Methodology

2.1. Additive manufacturing copper-tungsten-silver (Cu-W-Ag)

The additively manufactured filters were fabricated using Cu-W-Ag and SLM in-situ alloying. The atomised powders morphology is displayed in Fig. 1 at *wt.*% ratio of Cu-76%, W-17%, and Ag-7%. Cu and Ag are difficult to laser process due to their highly reflective and thermally conductive properties [40,42,57,58]. The high melt point of W also adds to the challenges for SLM [59,60]. However, although difficult to laser process all three materials have been successfully processed with varying success [41,61,62] with Cu seeing significant interest for various applications [63–65].

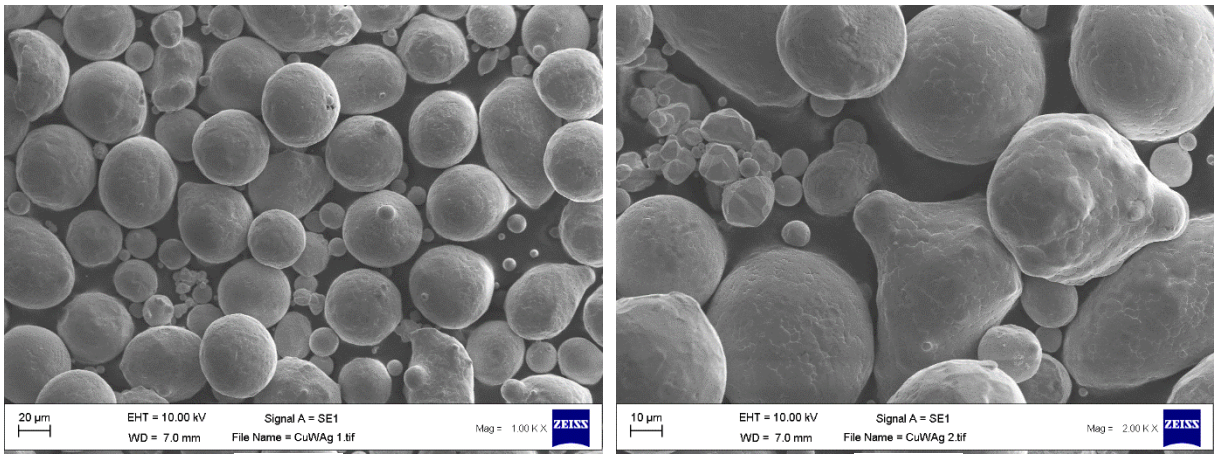

(a) **(b)**

Fig. 1. Scanning Electron Microscopy (SEM) data showing atomised Cu-W-Ag powders used for SLM in-situ alloying where (a) shows sphericity of the powder and (b) irregular morphology of some particles.

The anti-SARS-CoV-2 properties of Cu have been reported by Hutasoit [34], which informed the feedstock material composition to ascertain any improvement in antiviral effects from adding W and Ag as alloying elements. Fig 1a shows the spherical morphology of the powder required for the SLM process. Smaller satellite particles (~5µm) can be seen attached to the larger (~40µm) particles. Fig. 1b highlights some of the irregular morphology of some powder particles. Nevertheless, the overall sphericity and particle size range is favourable for the SLM process. All

samples were fabricated on an EOS M290 Powder Bed Fusion (PBF) AM system featuring a 400W laser with 100µm spot size. All builds were completed in an argon inert atmosphere with an oxygen content below 0.1%.

Physical 15 mm samples were 3D printed to satisfy and investigate all parametric combinations randomised by the surrogate model. Other than the process parameter variables the only CAD input was the global disk dimensions being 15 mm diameter and 2 mm thickness. The SLM process builds in a layer-by-layer fashion; after melting the first powder layer, the build platform was lowered by one 30 µm (layer thickness) increment so the next layer of powder could be deposited. The recoat dosing factor was kept at 150% to ensure sufficient Cu-W-Ag powder for each complete layer. The process build chamber was filled with 99.995% pure Argon at an oxygen content of 0.1% and a platform temperature of 35 °C. The samples were removed from the build platform using submerged wire Electro-Discharge Machining (EDM).

2.2. Selective laser melting and Standard Tessellation Language (STL)

SLM is a 3D printing technique that utilises a laser energy source to selectively melt metallic powders in a layer-by-layer fashion. The design freedom offered by SLM allows the realisation of complex geometries, which may not be feasible through more traditional manufacturing techniques [66,67]. As a result, SLM is in demand from the healthcare, automotive, aerospace, and electronics industries [68–70]. The SLM technique usually fabricates complex structures from CAD data generated in an STL file format.

The STL data format is currently the universally agreed format for 3D printing part geometry transfer. However, the process of CAD to STL conversion and slicing suitable for SLM includes multiple data conversion, complex support generation, file fixing, file slicing, and 3D printing build set up. While the process is relatively straight forward for a solid geometry, for porous geometries, the number of data points created increase exponentially in relation to feature size and porosity. This leads to significant challenges associated with pre-processing leading to alterations in the file format resolution, error fixing (bad edges, overlapping, intersecting triangles), and slicing parameter inconsistencies leading to print defects [71–73].

The complex conversion often requires specialist technicians and software experts increasing the processing time challenging the feasibility of redistributed manufacturing using 3D printing. To alleviate this problem, this study proposes an alternative methodology that simplifies the requirement of porous CAD geometry through a surrogate model featuring SLM process parameters. Despite the highly porous mesh developed in this study, the CAD simply informs the limits of the global geometry. As a result, the parametric combination proposed by the surrogate model can be used directly for a plug and play SLM parameter set for porous geometry fabrication.

2.3. Development of the surrogate model

2.3.1. SLM parameter influence for pore formation

The SLM process is complex due to having in excess of 130 feedstock and process variables [74], which includes the interaction between material absorptivity, reflectivity, laser diffusion, scattering, heat transfer, and material phase transformation [75]. The laser and material interactions affect the molten material melt pool during the SLM process. As such the processing parameters can have a significant impact on the resulting geometries being manufactured. Laser power, scan speed, layer thickness, and hatch distance all have a notable effect on energy density at the powder bed. As such they have a significant influence on heat transfer and phase transformation of the material affecting the stability of the melt pool [76].

The melted track size is therefore a function of the absorptivity and reflectivity of the material being processed and the energy input at the melt pool. The relationship between the SLM process parameters and the resulting melt track means that they can be manipulated to create controlled porous geometries. Usually, SLM process parameter development would study the influence of process parameters to develop a dense part. However, this study is concerned with identifying the process parameters influence in such a way as to create a porous mesh. To do this, the relationship between the SLM variables to fabricate Cu-W-Ag must be linked to the objective function of the geometry as represented in Eq. (1):

$$\begin{cases} f\ x\ = [f_1\ x\ , f_2\ x\ , \dots\dots , f_i\ x\ ] \\ s.t \qquad\qquad x^l \leq x \leq x^u \end{cases} \tag{1}$$

where $x = (x_1, x_2, \dots, x_k)$ is the vector of k process variables, x^l and x^u defines the minimum and maximum range of the process variables respectively for the objective function $f(x)$.

An objective function considering all the process parameter is not feasible as the SLM of Cu-W-Ag and the resulting track characteristics are not previously reported. However, for SLM in general, increasing scan speed reduces laser energy input leading to smaller weld pool and track width. Similarly when the scan speed is lowered, the increased exposure time leads to higher temperature at the melt pool consuming increased powder volume resulting in a wider melt pool [40]. Therefore, understanding the SLM parameter effects for optimum anti-SARS-CoV-2 filter fabrication is required.

Developing a controlled microporous architecture requires identifying the order of influence of the process parameters (variables) that leads to specific pore characteristics (responses). The methodology proposed in this study manipulates laser energy at the powder bed through SLM laser power (L_p), scan speed (S_s) and hatch distance (h_d) parameters applied in scan directions

laser track x and y to inform pore shape as shown in Fig. 2. The most favourable responses that characterise the pore shape considered are the track width (t_w), pore size in x (p_x) and y (p_y).

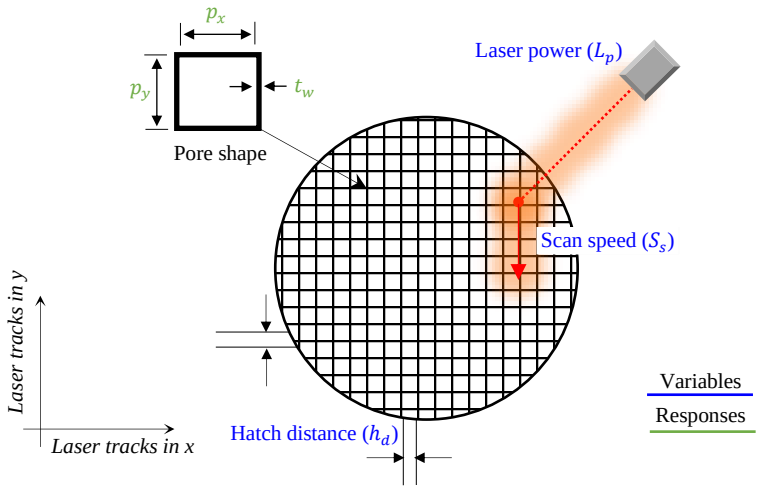

Fig. 2. SLM process parameters and responses used to develop anti-SARS-CoV-2 micropore filters without using porous CAD data.

2.3.2. Response surface model

The surrogate model employs the Response Surface Methodology (RSM) to identify the relationship between the process variables and the resulting responses of the Cu-W-Ag porous mesh geometry. The process parameters considered in this study are L_p, S_s, and h_d with associated ranges listed in Table 1. The selected ranges were informed by studies by Robinson *et al.* [40,42] investigating the laser melting of CuAg alloys where a 0.14 mm h_d resulted in a fully dense part. 1 mm h_d was selected to ensure visible pore size for initial RSM input. L_p ranged between minima and maxima of 320 and 370 W which is near the limits of the EOS PBF system utilised in this study. These parameters were selected based on existing literature [31,41] on reflective and thermally conductive materials while considering the high melt temperature of tungsten [59,77]. S_s ranged between minima and maxima of 250 and 500 mm/s which is relatively slow in comparison to current SLM materials. However, it is reasonable to assume that the relatively high melt temperature, thermal and reflective material properties require higher laser energy input at the powder bed for sufficient melt pool formation to take place.

Table 1. SLM process parameter variables and associated ranges considered for the Cu-W-Ag surrogate model.

Variables	Codes	-1	0	1
h_d (mm)	A	0.14	0.57	1
S_s (mm/s)	B	250	375	500
L_p (W)	C	320	345	370

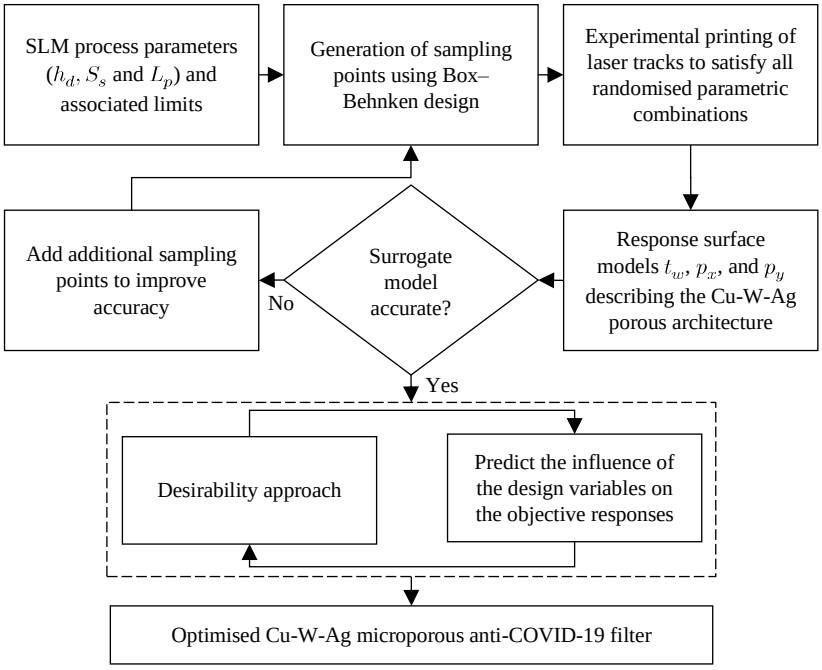

Fig. 3. The surrogate modelling approach used to derive the SLM process parameter informed porous Cu-W-Ag filter.

The Response Surface (RS) models were used to characterise t_w, p_x and p_y through conceiving empirical models that best fit the experimentally observed data. The resulting polynomial functions were used to predict the potential microporous architecture based on the order of influence of the contributing parameters. Once the model was trained using the experimental data sets, a desirability criterion was used to predict the optimum parametric combination that leads to the smallest pore size for the anti-SARS-CoV-2 filters. The surrogate model was also used to quantify the interaction effects of the process parameters and their influence on the Cu-W-Ag microporous architecture. Fig. 3 presents the summary of the surrogate modelling methodology used for the development of the optimal microporous Cu-W-Ag.

2.4. Response characterisation

2.4.1. Confocal microscopy

The responses considered in this study are the track width (t_w) and pore size measures in x (p_x) and y (p_y) as shown in Fig. 2. This response together dictates the overall porosity and pore size of the Cu-W-Ag microporous mesh. Post-printing the responses were characterised using an Olympus Lext OLS 3000 Laser Scanning Confocal Microscope (LSCM) and X-ray nano-tomography (nCT). This data-informed the surrogate model which was subsequently used to predict the optimum hatch distance, laser power, and scan speed parameters. The optimised parameters were then used to print the high-porosity mesh used for antiviral evaluation.

2.4.2. X-ray computed nano-tomography (nCT)

The Cu-W-Ag microporous architecture was characterised using nCT by evaluating the pore size and morphology. All analysis was carried out on the 'Bruker Skyscan 2211 X-ray nCT'. Nano-tomography is an emerging tool for the non-destructive analysis additively manufactured components and the enhanced resolution allows accurate characterisation of microporous features. The tomographs achieved are informed by the scanning and threshold parameters that can be set based on feature size allowing for high precision comparative analysis[78]. By setting the nCT scanning and threshold parameters are kept constant any variations in material density and porosity can be attributed to the process parameters and the feedstock material used for manufacturing. Accordingly, all Cu-W-Ag prototypes were scanned under identical nCT scanning, threshold, and reconstruction parameters to evaluate the influence of process parameters on the resulting microporous architecture [79,80].

2.5. Antiviral evaluation using a biosafe viral model of SARS-CoV-2

2.5.1. Phage phi6 host culture

Pseudomonas syringae from the DSMZ-German collection of microorganisms and cell cultures GmbH (reference DSM 21482), were cultured in solid Tryptic Soy Agar (TSA, Liofilchem). After that, the bacteria were incubated in Liquid Tryptic Soy Broth (TSB, Liofilchem) at 25ºC and 120 rpm.

2.5.2. Phage phi 6 propagation

Pseudomonas phage phi6 from the DSMZ-German collection of microorganisms and cell cultures (reference DSM 21518) was propagated according to the specifications provided.

2.5.3. Antimicrobial filter sample preparation

In addition to the 3D printed Cu-Ag-W microporous specimen, a non-woven spunlace fabric filter from NV EVOLUTIA (commercial filters used for face masks) of 10 mm in diameter was cut with a cylindrical punch to be used as reference material. All the discs were subsequently dried at 60º for 24 hours and sterilized by immersion in an absolute ethanol/distilled water solution (70/30% *v/v*) for 5 minutes at 25ºC and UV radiation one hour per each side.

2.5.4. Antiviral test

The antiviral activity of the samples was measured at 5 hours of contact with the biosafe virus model to ensure sufficient antimicrobial ion release. Thus, a volume of 50 µL of a phage suspension in TSB was introduced into each filter at a concentration of $1x10^6$ plaque-forming units per mL (PFU/mL) and allowed to incubate for 5 hours. After that each filter was placed in a falcon tube with 10mL TSB and sonicated for 5 minutes at 24 ° C and subsequently, vortexed for 1 minute. Serial dilutions of each falcon were performed for phage titration and 100

μL of each phage dilution were placed in contact with 100 μL of the host strain at OD_{600mm} = 0.5. The infective of the phage was measured by a procedure based on the double-layer method. Thus 4 mL of top agar (TSB + 0.75% bacteriological agar, Scharlau) and 5mM CaCl2 were introduced into the phage-bacteria mixture. The mixture was poured on TSA plates that were incubated for 24-48h in an oven at 25ºC.

3. Results and discussion

3.1. 3D printed Cu-W-Ag parametric filters

The as built SLM Cu-W-Ag samples based on the randomised process parameter combinations informed by the surrogate matrix are shown in Fig. 4. Upon completion of the build, the parts were removed from the build plate using Electrical discharge machining (EDM). As expected with SLM, a relatively rough surface finish was created due to the layer-by-layer AM process. Although the SLM process has numerous variables related to feedstock and laser-material interaction [74], identifying patterns in melt pool interaction was of primary importance.

Since the approach considered goes beyond pore resolution that is generally achievable from SLM, a comprehensive understanding of the melt track formation is critical in achieving a fine filter mesh. As shown in Fig. 5, the parametric combinations of laser power, scan speed, and hatch distance can generate Cu-W-Ag structures with varying degrees of porosity. Even though the porous samples validate the selection of the process parameters as suitable, the optimal combination of these parameters to print with fine pores is unknown. To establish such an optimum parametric combination, the order of influence of the process parameters is required. Accordingly, response surface models were generated based on the randomised variables.

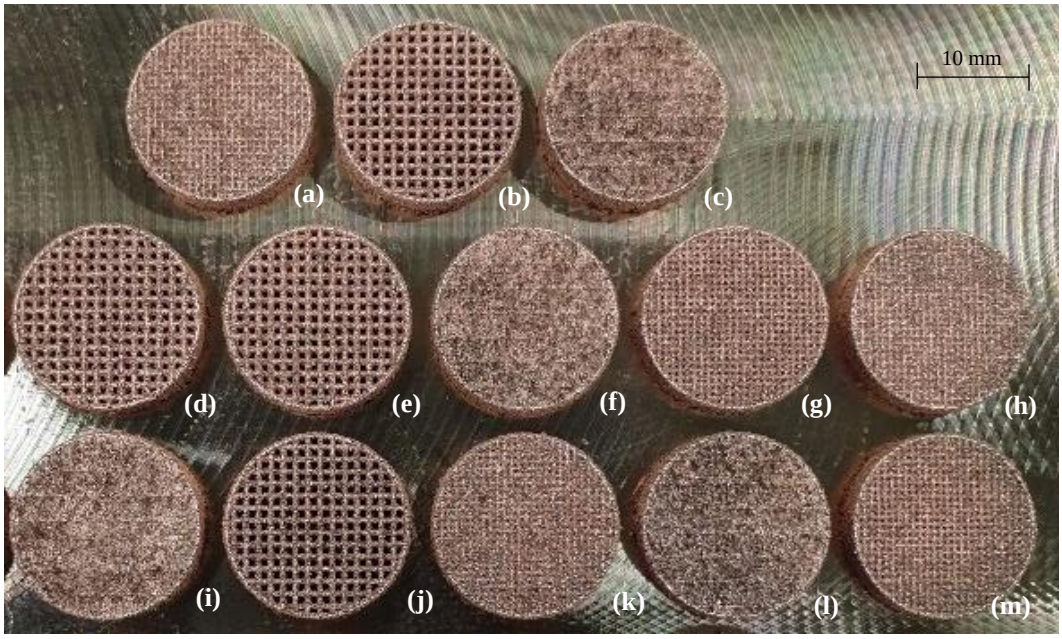

Fig. 4. Selective laser melted Cu-W-Ag samples based on randomised process parameter matrix generated to train the surrogate model. (a) $h_d = 0.57\ mm$, $S_s = 375\ mm/s$, $L_p = 345\ W$, (b) $h_d = 1\ mm$, $S_s = 500\ mm/s$, $L_p = 345\ W$, (c) $h_d = 0.14\ mm$, $S_s = 375\ mm/s$, $L_p = 370\ W$, (d) $h_d = 1\ mm$, $S_s = 250\ mm/s$, $L_p = 345\ W$, (e) $h_d = 1\ mm$, $S_s = 375\ mm/s$, $L_p = 370\ W$, (f) $h_d = 0.14\ mm$, $S_s = 375\ mm/s$, $L_p = 320\ W$, (g) $h_d = 0.57\ mm$, $S_s = 500\ mm/s$, (h) $L_p = 370\ W$, (h) $h_d = 0.57\ mm$, $S_s = 500\ mm/s$, $L_p = 320\ W$, (i) $h_d = 0.14\ mm$, $S_s = 250\ mm/s$, $L_p = 345\ W$, (j) $h_d = 1\ mm$, $S_s = 375\ mm/s$, $L_p = 320\ W$, (k) $h_d = 0.57\ mm$, $S_s = 250\ mm/s$, $L_p = 370\ W$, (l) $h_d = 0.14\ mm$, $S_s = 500\ mm/s$, $L_p = 345\ W$ and (m) $h_d = 0.57\ mm$, $S_s = 250\ mm/s$, $L_p = 320\ W$.

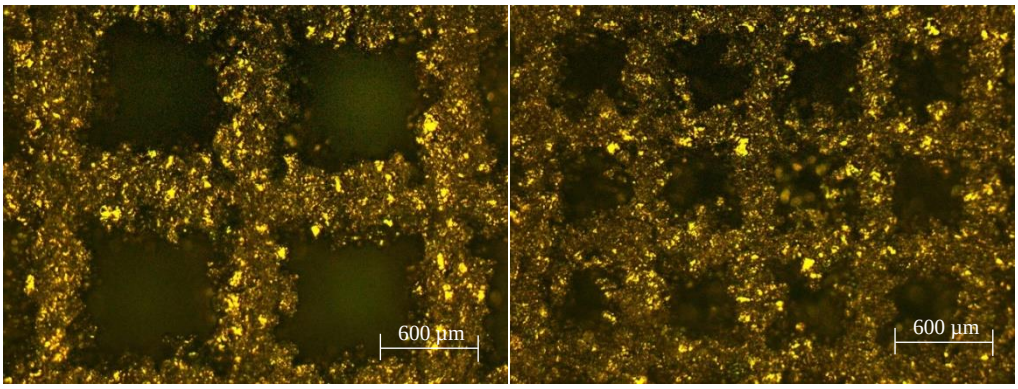

Fig. 5. Confocal microscopy showing the SLM process parameter informed porous architecture for a selection of the training samples where (a) $h_d = 1\ mm$, $S_s = 500\ mm/s$, $L_p = 345\ W$ and (b) $h_d = 0.57\ mm$, $S_s = 500\ mm/s$, $L_p = 345\ W$.

3.2. Surrogate model

Although it is established that the parametric combinations can result in porosity, their ideal combination to print the most optimum microporous architecture is unknown. Answering this

requires an understanding of both the interaction effects and order of influence of the process parameters in printing Cu-W-Ag for which the surrogate model is used. The process parameters that have the potential for significant influence on the porous architecture were identified as the hatch distance (h_d), scan speed (S_s) and laser power (L_p) with associated ranges as presented in Table 1. The surrogate model characterised the influence and interaction of these parameters on the track width (t_w), pore width (p_x) and pore height (p_y) of the microporous Cu-W-Ag. The result identified the SLM process parameters that had the most and least significance in printing an optimum microporous material.

The analysis of variance (ANOVA) technique was used to evaluate the accuracy of the surrogate model in characterising the microporous architecture. The validated model was used to navigate the response surface and quantify the relationship between the SLM process parameters (h_d, S_s, L_p) on the responses (t_w, p_x, p_y) characterising the printability and porosity of Cu-W-Ag. The approach followed the Box–Behnken higher-order response surface methodology conceiving the variables of interest as independent factors as listed in Table 2.

Table 2. Randomised training matrix informing the surrogate model for selective laser melting of Cu-W-Ag.

Variable factors			Responses (µm)		
$A = h_d$ (mm)	$B = S_s$ (mm/s)	$C = L_p$ (W)	t_w	p_y	p_x
1.00	500	345	367.20	624.04	667.59
0.57	375	345	349.86	331.06	324.22
0.14	375	370	379.85	0.00	0.00
0.57	500	370	314.40	246.95	294.19
0.14	375	320	379.85	0.00	0.00
1.00	250	345	453.41	547.96	586.32
1.00	375	370	389.18	569.65	560.77
0.14	250	345	453.41	0.00	0.00
0.57	500	320	291.64	308.93	295.88
0.57	250	370	409.10	249.82	248.55
0.57	250	320	291.15	295.06	290.88
1.00	375	320	379.85	627.19	615.07
0.14	500	345	367.20	0.00	0.00

The training responses were experimentally measured using confocal and nCT methodology with results as shown in Table 2. The statistical indices evaluating the performance of the surrogate model showed that both p_x and p_y (responses related to pore size) have a linear relationship with the process parameters as listed in Eqs. (2) and (3) respectively. Characterising the relationship of the Cu-W-Ag track width (t_w) to the SLM process parameters required a quadratic model as shown in Eqs. (4) indicating significant interaction effects between the variables.

$$p_x = 22.26 + 706.32h_d + 0.13S_s - 0.49L_p \quad (2)$$

$$p_y = 160.51 + 688.61h_d + 0.09S_s - 0.82L_p \quad (3)$$

$$t_w = -5524.61 - 429.91h_d + 2.24S_s + 31.86L_p - 1.46e^{-14}h_dS_s + 0.22h_dL_p - 7.62\ e^{-3}S_sL_p + 313.83{h_d}^2 + 1.55e^{-4}{S_s}^2 - 0.04{L_p}^2 \quad (4)$$

Table 3 shows the significant indices informed by ANOVA quantifying the accuracy of the surrogate model. The most establishes indexes in this regard includes the probability (p-value), coefficient of determination R^2, Adjusted R^2, and Adequate precision. The analysis of variance confirms significant F-value along with low p-values for all the three models indicating high model validity and negligible noise [81–83].

Table 3. Analysis of variance showing the significance and quality of the surrogate model developed.

Model	F-value	p-value	Statistical measurements		
			R^2	*Adj-R^2*	*Adeq-precision*
t_w	8.07	0.0059	0.9851	0.7990	9.9747
p_y	285.62	<0.0001	0.9893	0.9816	45.4985
p_x	384.18	<0.0001	0.9888	0.9863	52.0565

Generally, surrogate models that indicate a p-value <0.05 along with a >4 adequate precision ratio signifies highly accurate model with insignificant noise [84,85]. A closer to one R^2 is also referring to the high quality of the surrogate model being developed. Overall, the ANOVA demonstrates that all the models developed in this study are suitable for making valid predictions. This means that Eq. (2-4) adequately quantifies the relationship between the SLM process parameters and the characteristics of the Cu-W-Ag microporous architecture. Therefore, the surrogate model can be used to derive parametric combinations to print any targeted responses associated with microporous Cu-W-Ag.

3.3. Influence of SLM parameters on the Cu-W-Ag porous architecture

3.3.1. Parametric interaction and track width

SLM track width has a significant influence on the overall porosity that can be achieved. Therefore, when developing process informed microporous architecture using SLM, a critical understanding of the influence is required. Fig. 6 shows that scan speed and laser power have a higher influence on the Cu-W-Ag track width.

However, the order of influence and the interaction effects between the parameters vary significantly. Looking at the influence of S_s and h_d as shown in Fig. 6a, it can be seen that t_w increases almost linearly as S_s decreases resulting in the thinnest track width at the highest scan speed. As such the interaction effects between S_s and h_d on Cu-W-Ag track width is insignificant. This was expected as the characteristics of track width in SLM are primarily attributable to the

laser energy density where the hatch distance generally has a smaller influence. A similar trend was displayed when evaluating the interaction effects of L_p and S_s as shown in Fig. 6b. It can be seen that track width is significantly influenced by laser power with negligible interaction from h_d. The track width can be found to increase with a rise in L_p and flattening out at high laser powers. This flattening effect close to high L_p can be interpreted as no further variation in track width once the required energy for complete melting is reached. The track width reduced almost linearly as the laser-powered reduced from 350 to 320 W leading to the thinnest t_w at the lowest L_p of 320 W.

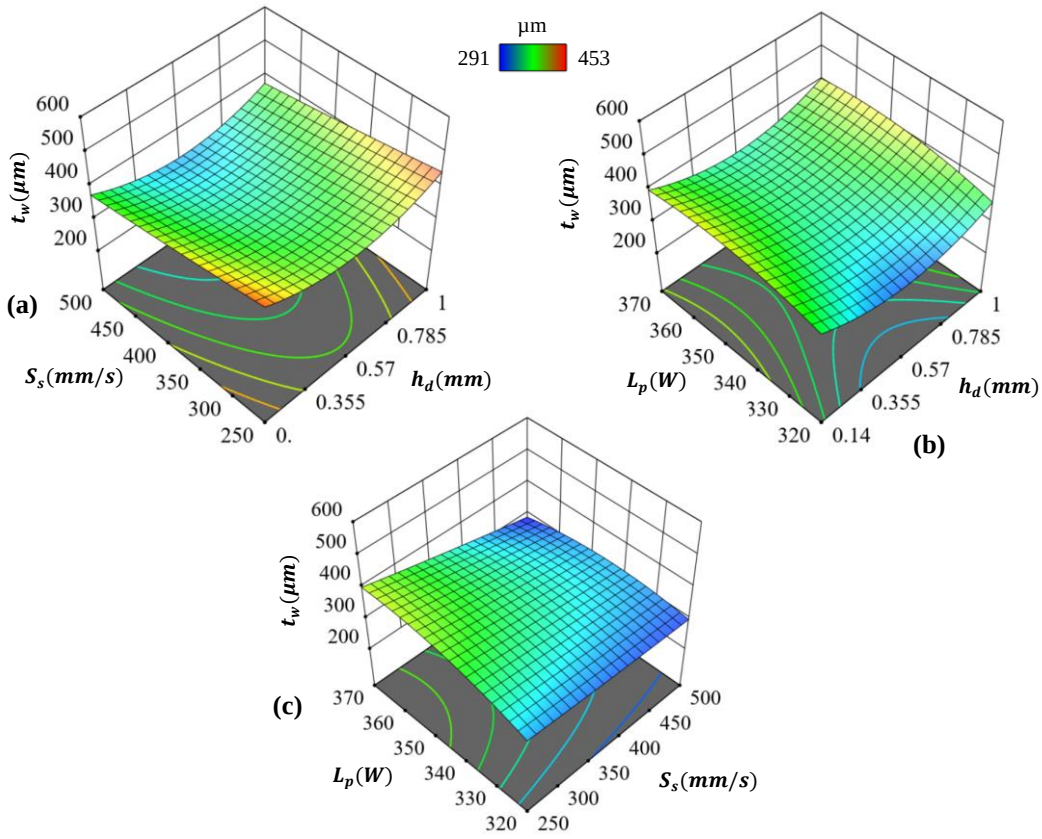

Fig. 6. Influence of the SLM process parameters on printed Cu-W-Ag track width showing (a) the influence of S_s and h_d when L_p is constant, (b) the influence of L_p on h_d when S_s is constant and (c) the influence of L_p and S_s when h_d is constant. The comparison of (a), (b), and (c) also reveals the interaction effects between the design parameters taking place.

Overall, the Cu-W-Ag track width is primarily controlled by laser power and scan speed as shown in Fig. 6c with significant interaction effects between the two parameters were achieving the thinnest t_w required careful control over both S_s and L_p. The largest track width was observed at high laser power and low scan speeds. Looking at the order of influence, the most significant terms on t_w are the interaction effects of S_s and L_p in the order $L_pS_s > S_s > L_p$ with the least influence from h_d. This means that to generate a highly microporous Cu-W-Ag

architecture informed by process parameters a higher scan speed and lower laser power that induces sufficient energy density for a thinner but fully melted track width is required.

3.3.2. Influence on pore size

The pore size of the Cu-W-Ag printed filters are characterised using the responses p_x and p_y referring to the overall size of the individual porous mesh. Fig. 7 shows that the pore geometry of laser melted samples are primarily dependent on the hatch distance (Fig. 7a and 7c) with no influence from scan speed or laser power (Fig. 7b and 7d). The dependency of p_x and p_y on h_d is also linear with the lowest and highest pore sizes relating to the lowest and highest h_d respectively. This response is expected as the key SLM parameter modulating the distance between two adjacent tracks in SLM is hatch distance.

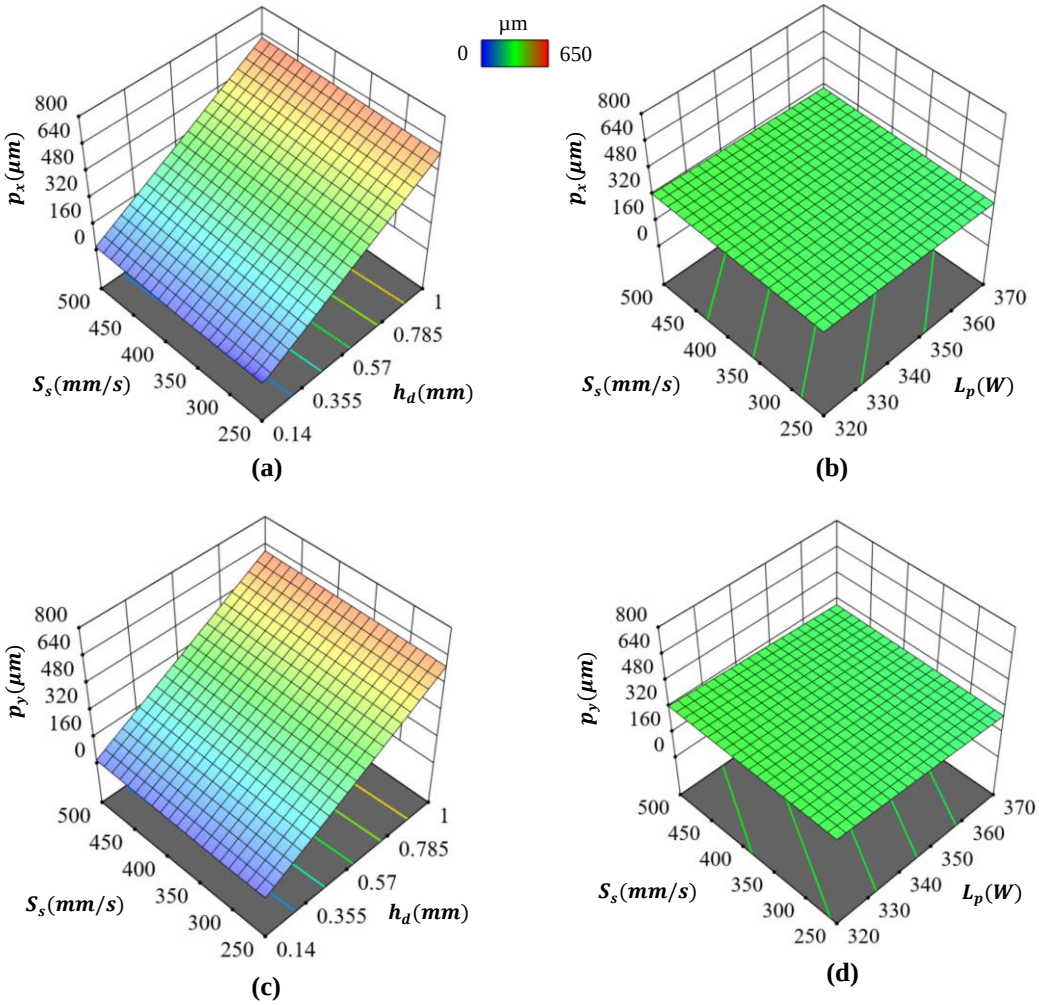

Fig. 7. Influence of SLM process parameters on the pore size of printed Cu-W-Ag microporous mesh showing (a) the influence of S_s and h_d on p_x when L_p is constant, (b) the influence of S_s and L_p on p_x when h_d is constant, (c) the influence of S_s and h_d on p_y when L_p is constant, (d) the influence of S_s and L_p on p_y when h_d is constant.

Neither the variation in S_s or L_p can introduce any significant changes in pore size, which was expected as the pore size is primarily dictated by the distance between two Cu-W-Ag tracks.

The limited interaction between S_s or L_p can be further validated using Fig. 7b and 7C, where the trend in performance with varying S_s and L_p while keeping h_d constant has no effect. This results in an almost flat performance slope resulting in similar p_x and p_y despite the changes in S_s or L_p. Overall, the most significant term dictating the Cu-W-Ag pore size are the first-order effects of h_d.

The influence of process parameters on both track width and pore sizes of the printed Cu-W-Ag reveals that the interaction effects can be used to simplify the 3D printing of metal microporous architecture. As such, targeted porosity and pore size can be achieved by carefully modulating the process parameters allowing ease of customisability, and scalability. Since the interaction and influence of all three SLM process parameters on the microporous architecture have been established, the next step is to derive the most optimal parametric combination using the surrogate model to print an ultrafine Cu-W-Ag microporous mesh ready for antiviral testing. Based on the analysis so far it is clear that a highly porous architecture can be developed by minimising L_p, increasing S_s and reducing h_d resulting in thinner tracks as close as possible but not so close as to introduce track interaction and a potentially dense part.

3.4. Optimum Cu-W-Ag microporous filters

Although the influence of the process parameters on the characteristics of printed of Cu-W-Ag have been established, the optimum combination of parametric values that leads to an optimum microporous architecture are still unknown. Accordingly, a problem description targeting the ideal characteristics of the Cu-W-Ag microporous architecture is required to generate an optimum filter. This is completed through the development of a multi-objective description of the optimisation problem. An optimum Cu-W-Ag microporous filter should be able to provide a large surface area while featuring stable and consistent tracks. In other words, the optimised structure should allow for the smallest p_x and p_y without producing a dense structure while exhibiting the thinnest stable track width (t_w). A balance of these three parameters will allow the Cu-W-Ag mesh to generate a microporous architecture with a small pore size but with large overall porosity and therefore large contact area to allow a maximum surface for antiviral activity. Therefore, the objectives were to minimise p_x and p_y (to a positive integer that is not zero) while also minimising t_w. The resulting optimisation problem can be formulated as shown in Eq. (5):

$$\begin{cases} Minimise\ t_w = f_1(h_d, S_s, L_p) \\ Minimise\ p_x = f_2(h_d, S_s, L_p) \\ Minimise\ p_y = f_3(h_d, S_s, L_p) \\ \\ s.t \quad 0.14 \le h_d \le 1 \\ s.t \quad 250 \le S_s \le 500 \\ s.t \quad 320 \le L_p \le 370 \end{cases} \tag{5}$$

The desirability approach was the optimisation methodology of choice due to the multi-objective nature of the problem [86]. The desirable function was conceived by representing the objective function (D) the meets the desirable range for each response (d_i). As such the least and most desirable outcomes are represented 0 and 1 respectively. When n is the number of responses, the multi-objective function is a geometric mean of all transformed responses as shown in Eq. (6):

$$D = (d_1 \cdot d_2 \cdot \ldots \cdot d_n)^{\frac{1}{n}} = \left(\prod_{i=1}^{n} d_i\right)^{\frac{1}{n}} \quad (6)$$

For the multi-objective optimisation problem considered, each response is assigned a low and high value as shown in Eq. (5) which is solved using the desirability criterion. The results are shown in Fig. 8 as a function of the desirability objective considering all interaction effects. As shown in Fig. 8a, the optimal solution is at the highest desirability of 0.95 at high scan speed, low laser power, and at a hatch distance of 0.4 mm.

It should be noted that although the desirability criteria for minimising the pore size is given this value should be slightly above the powder dimensions. This was set to prevent the powder particles from getting stuck in the pores leading to a dense part. As can be seen from Fig. 8b, despite keeping the other parameters constant increasing the laser power decreases the desirability. Overall, the lowest desirable solution is at the lowest scan speed, hatch distance, and highest laser power as shown in Fig. 8c. Table 4 shows one of the parametric combinations that offer the highest desirability that was used to fabricate the Cu-W-Ag microporous architecture for antiviral testing.

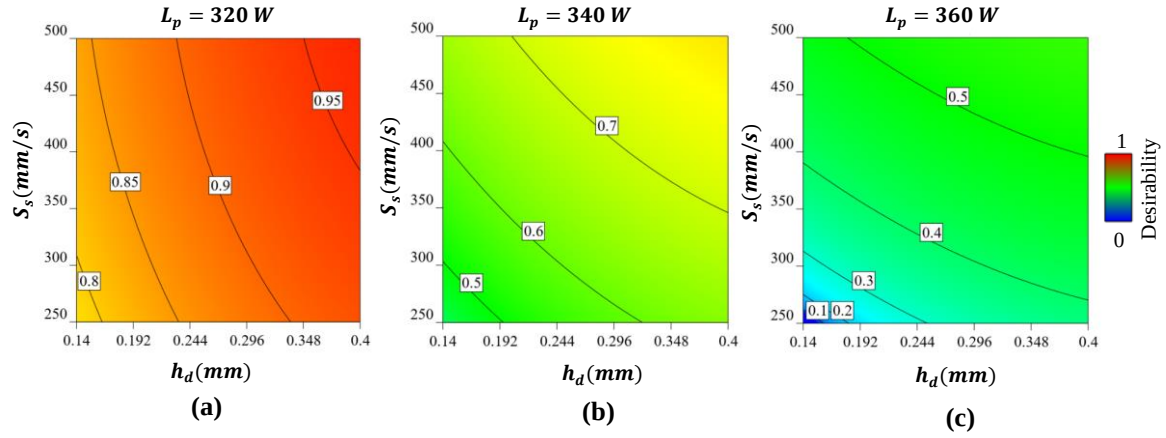

Fig. 8. The desirability of the optimum solution for the Cu-W-Ag microporous architecture against the SLM process variables showing (a) the effect of scan speed and hatch distance at a laser power of 320 W (b) the effect of scan speed and hatch distance at a laser power of 340 W and (c) the effect of scan speed and hatch distance at a laser power of 360 W. A desirability contour of 0.0 and 1.0 refers to the least and most optimum solution respectively that can be achieved between the parametric SLM process ranges considered.

Based on the predicted process parameters, Cu-W-Ag samples were manufactured (Fig. 9a), and nCT (Fig. 9b) evaluation carried out as shown in Fig. 9. nCT was used to analyse sample

morphology with 3D visualisations displayed in Fig. 9b indicating relatively dense material (high X-ray absorption) at the tracks. The SLM parametric combination was able to deliver a stable Cu-W-Ag porous architecture.

Table 4. Optimal process parameters predicted for Cu-W-Ag microporous mesh by the surrogate model.

Number	h_d (mm)	S_s (mm/s)	L_p (W)	Desirability
1	0.4	500	320	0.95

A density gradient was observed around the pores with a clear porous architecture displaying an average pore size of around 80 µm. Any further reduction in pore size runs the risk of feedstock powder particles becoming embedded in the porous architecture creating a dense part. This suggests the potential limits for this material composition, powder particle size, and SLM laser spot size. The material around the pores can be seen to be uniformly dense throughout the part as shown in Fig. 9b validating the suitability of the process parameters. Overall, the results from the experimentally measured optimum Cu-W-Ag microporous mesh in comparison to the surrogate model were in good agreement as shown in Table 5. The potential bottleneck in further reducing the pore size is associated with the particle size distribution of the feedstock. Any further increase in the porosity resolution requires the fabrication of thinner tracks which will require the use of lower particle size.

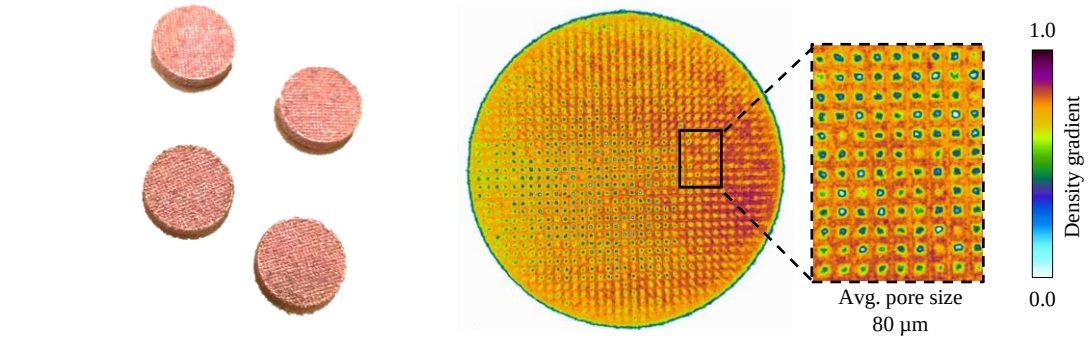

Fig.9. Manufactured optimum Cu-W-Ag microporous filters based on process parameter combination predicted by the surrogate model where (a) is manufactured antiviral samples and (b) is nCT 3D visualisation of microporous morphology.

The surrogate model underestimated the track width and pore size in x by 3% and 3.9% respectively. For the pore size in y, the surrogate model overestimated the prediction by 4.8% in comparison to experimentally measured results. Overall, the results show that the Cu-W-Ag microporous mesh is the best achievable using the powder characteristics considered. As such, any further refinement in the porous architecture requires finer feedstock powder. Accordingly, the optimised porous architecture was used for antiviral evaluation to characterise its performance against the SARS-CoV-2 viral model to evaluate its suitability for a porous mask filter prototype.

Table 5. Confirmation runs for optimum Cu-W-Ag microporous structure.

Item	$t_w(\mu m)$	$p_x(\mu m)$	$p_y(\mu m)$
Surrogate	292	77	84
Actual	301	80	80
% difference	3.0%	3.9%	4.8%

3.5. Antiviral performance against SARS-CoV-2

The optimised Cu-W-Ag microporous mesh was evaluated against the biosafe viral model of SARS-CoV-2 and the results are summarised in Table 6. Visual data of the experiments were collected after 5 hours of contact with the phages as shown in Fig. 10. As expected, the commercial filter used as reference material (Fig. 10c) and the control sample (Fig. 10b) resulted in no antiviral activity under identical experimental conditions (~0% of antiviral activity). In comparison, the 3D printed Cu-W-Ag microporous filters showed strong antiviral activity (100% of viral inhibition) after 5 hours of contact as shown in Fig. 10a. After 5 hours of contact, no plaques can be observed.

Table 6. Titration after double-layer assay. Titer in PFU per ml of control, commercial face mask filters, 3D Cu-W-Ag filters, and % antiviral activity at 5 hours with respect to control.

Sample	Titer (PFU/mL) at 5 hours	% Antiviral activity at 5 hours
Control	$4.56\times10^6 \pm 3.97\text{x}10^5$	-
Commercial face mask filter	$4.48\times10^6 \pm 3.66\text{x}10^5$	~0.1%
Printed Cu-W-Ag filter	0	100%

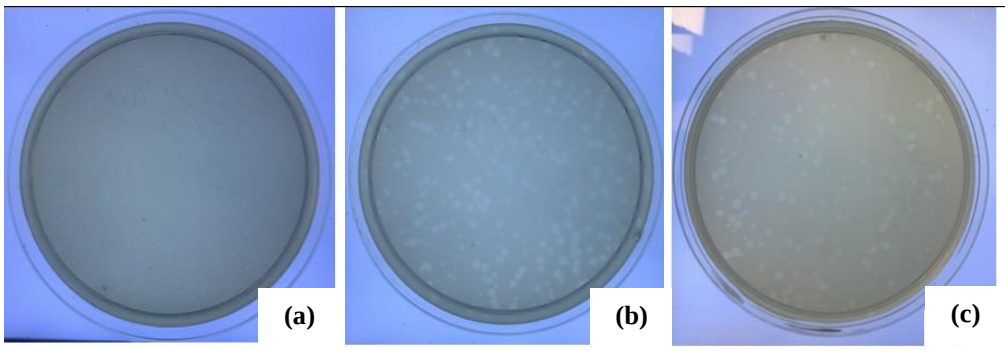

Fig. 10. Loss of phage phi 6 viability measured by the double-layer method at 10^{-1} dilution: (a) phages in contact with Cu-W-Ag filter for 5 hours, (b) control sample (phage not treated with any filter) for 5 hours and (c) phages in contact with the commercial filter used as reference material for 5 hours.

The phage titer of each type of filter was compared with the results obtained by adding 50 µL of phage to the bacteria without being in contact with any sample and without performing sonication-vortex (control) to determine the antiviral activity (%) of the samples by applying Eq. 7 (see results in Table 6), where *Titer* is expressed in PFU/mL. Table 6 shows

when the viruses are in contact with the printed Cu-W-Ag filters for 5 hours, a strong viral inactivation is produced (100%) in comparison to the control and commercial face mask filter samples.

$$\% \; Antiviral \; activity = \; 100 - \frac{\log \; 1 + Titer \; _{sample}}{\log \; Titer \; _{control}} \cdot 100 \tag{7}$$

3.6. Cu-W-Ag anti-SARS-CoV-2 proof of concept prototype

Having established optimum SLM parameters and the antiviral effectiveness of Cu-W-Ag microporous architecture, an initial proof-of-concept is conceived under dimensions satisfying the 'copper3D' open-source model shown in Fig.11. The global dimensions of the novel Cu-W-Ag antiviral filter were conceived to fit the open-source Copper3D mask as shown in Fig. 11c. To achieve this the pre-processing is simplified through the machine-centric algorithmic approach described using the multi-objective design criterion.

The printed samples were informed by the optimised process parameters developed and resulted in an identical process architecture as shown in Fig. 12. It is important to note that the research presented has numerous applications and this is only one potential application. Furthermore, a microporous architecture such as the one developed in this research is highly complex if traditional CAD pre-processing is required. As such the technique confirms the potential for the redistributed manufacturing of antiviral Cu-W-Ag microporous architecture without the need for a porous CAD informing the SLM process.

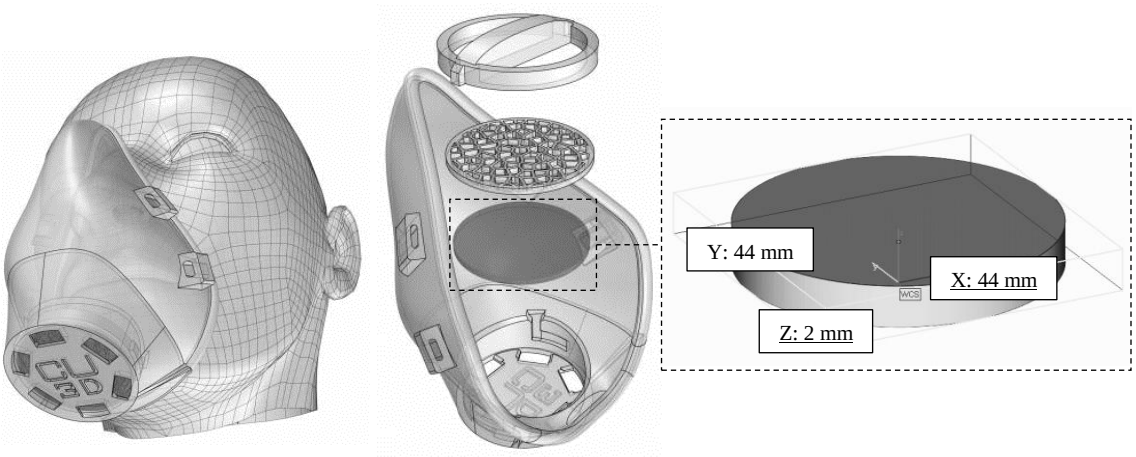

Fig. 11. The global dimensions of the Cu-W-Ag antiviral filter were designed to fit the Copper3D open-source 3D printable mask. (a) A representative example of how the mask fits on the face, (b) showing the exploded assembly view with various compartments, and (c) the global dimensions of the porous Cu-W-Ag antiviral filter conceived in this study. The authors chose to mimic the replaceable filter from the Copper3D open-source mask as the antiviral filter can be manufactured using the procedure mentioned in this paper ready for further testing.

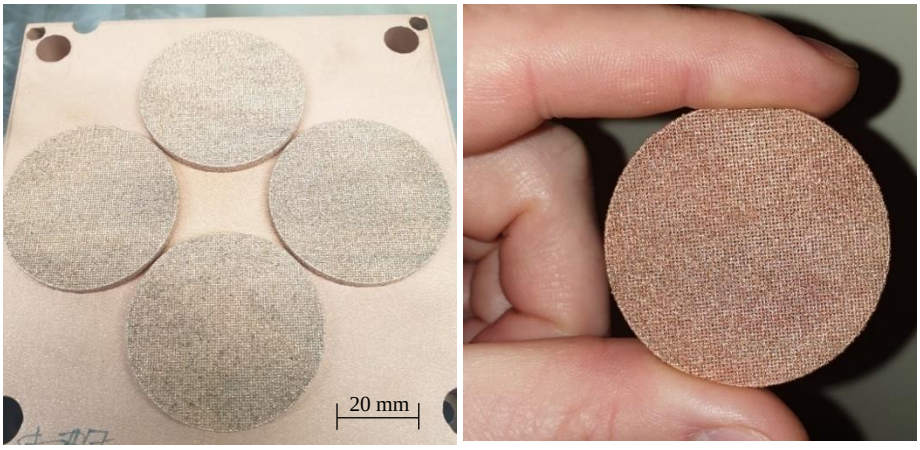

(a) **(b)**

Fig. 12. 3D printed Cu-W-Ag SARS-CoV-2 antiviral microporous filters developed using the SLM process informed technique suitable for the open-source Copper3D mask. (a) Four filter samples as built on a copper substrate (b) one filter removed from the build platform using EDM showing the microporous architecture.

Although a potential proof-of-concept for a particular application is demonstrated, the aim of this research was not to develop a final product. Instead, it is the first step in establishing on demand 3D printing of microporous materials with exponentially large contact surfaces that maximise antimicrobial activity without the need for complex CAD based data manipulation. As such the project initiate a new direction which fellow researchers can adapt and improve to develop functional biomedical and antiviral biomaterials. For the mask prototype, further research is necessary to identify suitable breathability and bacterial filtration efficiency required for their mass production and commercialization according to the European standard for community face coverings (CWA 17553:2020).

4. Prospects and challenges

4.1. Pandemic preparedness

Previous epidemics have expanded human knowledge resulting in techniques to combat pathogenic infectious diseases [87]. However, at the time of writing (Dec. 2020) the COVID-19 pandemic had reported 54 million cases with more than 1 million confirmed deaths globally [88]. The international crisis has highlighted the continued danger to human health and world economies from emerging novel respiratory virus infections [89,90] but also the requirement for future pandemic preventative measures.

Additionally, antibiotic resistance is known to be increasing and therefore alternative antimicrobial techniques are required. As discussed, antimicrobial materials offer the potential for antibacterial [31], antifungal, and antiviral applications [30] and could offer the potential to be tailored to combat specific pathogenic infectious diseases due to the various antimicrobial mechanisms. However, the exact mechanisms for antimicrobial properties are yet to be fully

understood and more research is required. In this respect, metallic ion release and the effect on antimicrobial mechanisms should be an area of future investigations.

The redistributed manufacturing methodology proposed in this study reports the potential for the removal of transportation and supply chain constraints and therefore the antimicrobial effects of currently readily available 3D printing materials should see further investigations. Combining the digitalisation of antimicrobial materials and components through redistributed 3D printed manufacturing offers significant potential for future fabrication of antiviral surfaces, wound dressings, pin site infections, and face visors and masks.

4.2. Process parameter informed porous architecture

The move away from STL informed porosity reduces the resolution of CAD data required for the printing process. This approach simplifies the number of geometrical data points reducing the computational cost improving the overall print efficiency. The use of SLM process parameters to inform the size and shape of the pores also allow the data to be transferred directly to any compatible 3D printers where the CAD data is only required for the global dimensions. This in turn reduces the need for expensive CAD manipulation hardware and specialist personnel to deal with large STL data points. The approach reduces data storage and large file transfer requirements enhancing the print on-demand redistributed manufacturing and mass personalisation of the global geometry. While the method enhances the versatility of achievable pore sizes and track widths, their suitability to print complex pore shapes are yet to be established. Furthermore, the SLM parametric combination informed by the surrogate model is highly dependent on both the composition and particle characteristics of the powder bed. As such they are not transferable for the generation of similar porous architecture in a different material. Overall, the approach of using surrogate models to conceive porous materials is in its infancy and further research is required to enable its application to a wider range of materials and pore architecture.

4.3. Regulation and approval

Additive manufacturing such as selective laser melting (SLM) is already being used in the biomedical industry and is widely considered the key enabling technology for the future of personalised medicine. Although significant progress has been made in the arena of 3D printed biomedical products, the regulatory process is still evolving [91–93]. However, it is hopeful that Class I devices such as the ones demonstrated in this study can be approved through an existing well-established process. This is because materials used for Class-I devices are only suitable for external contact similar to bandages and masks [33]. To use the novel Cu-W-Ag material developed in this study for Class II and III devices requires further testing both *in vivo* and *in vitro*. This is where semi-molten particles or residual powder can inhibit biocompatibility, needing further post-processing and testing to meet targeted quality criteria. The novelty of the

material also means that further test data from both clinical and non-clinical studies will be required before they become commonly place for Class II and III devices. There is also the requirement for medical compliance of manufacturing facilities and establishing quality control strategies that are also critical [94].

Despite the class of approval, the use of process parameters to inform pore size and pore geometry demonstrated in this study outperforms conventional methods both from a cost and quality perspective. This is because the conventional AM technique relies on large STL data points to represent the pore architecture in addition to the global part dimensions, which requires multiple data conversion, complex support generation, file fixing, slicing and orientation. While the process is relatively straight forward for a solid geometry, for porous geometries, the number of data points increase exponentially in line with the resolution of the porous architecture required. This leads to significant challenges associated with pre-processing, leading to alterations in the file format resolution, error fixing (bad edges, overlapping, intersecting triangles), and slicing parameter inconsistencies leading to print defects when using conventional technique [71–73,95]. The excellent agreement between predicted and actual data also shows the accuracy and consistency of the parameter informed technique, which is also a challenge when working with high resolution STL files with large data points.

5. Conclusion

This study proposes a redistributed manufacturing methodology to 3D print Cu-W-Ag anti-SARS-CoV-2 material and microporous morphology. The addition of W and Ag as alloying elements to Cu is established for the first time resulting superior antiviral properties compared to Cu coated stainless steel which resulted in 99.2% virus inactivation after 5 hours. The Selective Laser Melting (SLM) process informed methodology allows 3D printing to be carried out close to the end-user by simplifying the need for complex Computer Aided Design (CAD) pre-processing that transcends current supply chain limitations. The methodology reduces the requirements for data-intensive, complicated, and time-consuming CAD while removing the potential for manufacturing errors from geometry, support, and slicing software through SLM process parameter methodology. This is achieved through the development of a surrogate model resulting in optimum SLM processing parameters for Cu-W-Ag. It was found that the most significant parameters for Cu-W-Ag track width were the interaction effects of scan speed (S_s) and laser power (L_p) in the order $L_pS_s > S_s > L_p$. For pore size (p_x and p_y), hatch distance (h_d) has the most significant effect. The optimised Cu-W-Ag microporous materials showed 100% viral inactivation against the *Pseudomonas* phi 6 phage used as enveloped RNA viral model of SARS-CoV-2. As such Cu-W-Ag microporous material is suitable to reduce surface contamination and the spread of COVID-19. The evolution of this and future pandemics will bring unexpected situations where the preparedness in conceiving and on-site 3D printing of antiviral materials can achieve rapid solutions. Although this research was concerning the

development of a Cu-W-Ag antiviral material, the approach can be transferred to develop functional biomaterials that can be digitally transported, and 3D printed close to point-of-care. As such this work is the first to propose an application-specific redistributed manufacturing methodology suitable for microporous antiviral material offering a new direction for 3D printing functional materials.

Acknowledgements

This research was conducted with support from European Commission and EOS GmbH.

Data availability

The data that supports the findings of this study are available from the corresponding author upon reasonable request.

References

[1] C. Carter, J. Notter, COVID-19 disease: a critical care perspective, Clin. Integr. Care. 1 (2020) 100003. https://doi.org/10.1016/j.intcar.2020.100003.

[2] A. Arjunan, S. Zahid, A. Baroutaji, J. Robinson, Journal of the Mechanical Behavior of Biomedical Materials 3D printed auxetic nasopharyngeal swabs for COVID-19 sample collection, J. Mech. Behav. Biomed. Mater. (2020) 104175. https://doi.org/10.1016/j.jmbbm.2020.104175.

[3] D. Pradhan, P. Biswasroy, P. Kumar Naik, G. Ghosh, G. Rath, A Review of Current Interventions for COVID-19 Prevention, Arch. Med. Res. 51 (2020) 363–374. https://doi.org/10.1016/j.arcmed.2020.04.020.

[4] M.Y. Yen, J. Schwartz, C.C. King, C.M. Lee, P.R. Hsueh, Recommendations for protecting against and mitigating the COVID-19 pandemic in long-term care facilities, J. Microbiol. Immunol. Infect. 53 (2020) 447–453. https://doi.org/10.1016/j.jmii.2020.04.003.

[5] M. Lotfi, M.R. Hamblin, N. Rezaei, COVID-19: Transmission, prevention, and potential therapeutic opportunities, Clin. Chim. Acta. 508 (2020) 254–266. https://doi.org/10.1016/j.cca.2020.05.044.

[6] M. Mhango, M. Dzobo, I. Chitungo, T. Dzinamarira, COVID-19 Risk Factors Among Health Workers: A Rapid Review, Saf. Health Work. 11 (2020) 262–265. https://doi.org/10.1016/j.shaw.2020.06.001.

[7] İ. Devrim, N. Bayram, Infection control practices in children during COVID-19 pandemic: Differences from adults, Am. J. Infect. Control. 48 (2020) 933–939. https://doi.org/10.1016/j.ajic.2020.05.022.

[8] R. Chakraborty, S. Parvez, COVID-19: An overview of the current pharmacological interventions, vaccines, and clinical trials, Biochem. Pharmacol. 180 (2020) 114184. https://doi.org/10.1016/j.bcp.2020.114184.

[9] J. Hellewell, S. Abbott, A. Gimma, N.I. Bosse, C.I. Jarvis, T.W. Russell, J.D. Munday, A.J. Kucharski, W.J. Edmunds, F. Sun, S. Flasche, B.J. Quilty, N. Davies, Y. Liu, S. Clifford, P. Klepac, M. Jit, C. Diamond, H. Gibbs, K. van Zandvoort, S. Funk, R.M. Eggo, Feasibility of controlling COVID-19 outbreaks by isolation of cases and contacts, Lancet Glob. Heal. 8 (2020) e488–e496. https://doi.org/10.1016/S2214-109X(20)30074-7.

[10] V. Jain, K. Gupta, K. Bhatia, A. Bansal, S. Arora, A.K. Khandelwal, J.R. Rosenberg, J.P. Levisay, C.L. Tommaso, M.J. Ricciardi, A. Qamar, Management of STEMI during the COVID-19 pandemic : Lessons, Trends Cardiovasc. Med. c (2021) 1–6. https://doi.org/10.1016/j.tcm.2020.12.003.

[11] D. Bradley, Copper against Covid, Mater. Today. xx (2020) 7021. https://doi.org/10.1016/j.mattod.2020.09.016.

[12] M.R. De Georgeo, J.M. De Georgeo, T.M. Egan, K.P. Klee, M.S. Schwemm, H. Bye-Kollbaum, A.J. Kinser,

Containing SARS-CoV-2 in hospitals facing finite PPE, limited testing, and physical space variability: Navigating resource constrained enhanced traffic control bundling, J. Microbiol. Immunol. Infect. (2020). https://doi.org/10.1016/j.jmii.2020.07.009.

[13] A.W.H. Chin, J.T.S. Chu, M.R.A. Perera, K.P.Y. Hui, H.-L. Yen, M.C.W. Chan, M. Peiris, L.L.M. Poon, Stability of SARS-CoV-2 in different environmental conditions, The Lancet Microbe. 1 (2020) e10. https://doi.org/10.1016/s2666-5247(20)30003-3.

[14] A.A. Cortes, J.M. Zuñiga, The use of copper to help prevent transmission of SARS-Coronavirus and Influenza viruses. A general Review, Diagn. Microbiol. Infect. Dis. 98 (2020) 115176. https://doi.org/10.1016/j.diagmicrobio.2020.115176.

[15] S. Furka, D. Furka, N.C.T.C.T. Dadi, P. Palacka, D. Hromníková, J.A. Dueñas Santana, J.D. Pineda, S.D. Casas, J. Bujdák, Novel antimicrobial materials designed for the 3D printing of medical devices used during the COVID-19 crisis, Rapid Prototyp. J. 27 (2021) 890–904. https://doi.org/10.1108/RPJ-09-2020-0219.

[16] F.D. Cojocaru, D. Botezat, I. Gardikiotis, C.M. Uritu, G. Dodi, L. Trandafir, C. Rezus, E. Rezus, B.I. Tamba, C.T. Mihai, Nanomaterials designed for antiviral drug delivery transport across biological barriers, Pharmaceutics. 12 (2020) 1–34. https://doi.org/10.3390/pharmaceutics12020171.

[17] S. Galdiero, A. Falanga, M. Vitiello, M. Cantisani, V. Marra, M. Galdiero, Silver nanoparticles as potential antiviral agents, Molecules. 16 (2011) 8894–8918. https://doi.org/10.3390/molecules16108894.

[18] A. Arjunan, A. Baroutaji, J. Robinson, A.-G. Olabi, Smart Tribological Coating, in: Ref. Modul. Mater. Sci. Mater. Eng., Elsevier, 2021. https://doi.org/https://doi.org/10.1016/B978-0-12-815732-9.00113-3.

[19] A.S. Praveen, A. Arjunan, A. Baroutaji, Coatings for Dental Applications, in: Ref. Modul. Mater. Sci. Mater. Eng., Elsevier, 2021. https://doi.org/https://doi.org/10.1016/B978-0-12-815732-9.00114-5.

[20] B. Begines, A.L. Hook, M.R. Alexander, C.J. Tuck, R.D. Wildman, Development, printability and post-curing studies of formulations of materials resistant to microbial attachment for use in inkjet based 3D printing, Rapid Prototyp. J. 22 (2016) 835–841. https://doi.org/10.1108/RPJ-11-2015-0175.

[21] C. Wu, Y. Zhou, M. Xu, P. Han, L. Chen, J. Chang, Y. Xiao, Copper-containing mesoporous bioactive glass scaffolds with multifunctional properties of angiogenesis capacity, osteostimulation and antibacterial activity, Biomaterials. (2013). https://doi.org/10.1016/j.biomaterials.2012.09.066.

[22] I.M. Hamouda, Current perspectives of nanoparticles in medical and dental biomaterials, J. Biomed. Res. (2012). https://doi.org/10.7555/JBR.26.20120027.

[23] F. Paladini, M. Pollini, A. Sannino, L. Ambrosio, Metal-based antibacterial substrates for biomedical applications, Biomacromolecules. (2015). https://doi.org/10.1021/acs.biomac.5b00773.

[24] J.S. Walker, J. Arnold, C. Shrestha, D. Smith, Antibacterial silver submicron wire-polylactic acid composites for fused filament fabrication, Rapid Prototyp. J. 26 (2020) 32–38. https://doi.org/10.1108/RPJ-04-2019-0100.

[25] S. Li, S. Dong, W. Xu, S. Tu, L. Yan, C. Zhao, J. Ding, X. Chen, Antibacterial Hydrogels, Adv. Sci. 5 (2018). https://doi.org/10.1002/advs.201700527.

[26] H. Sashiwa, S.I. Aiba, Chemically modified chitin and chitosan as biomaterials, Prog. Polym. Sci. (2004). https://doi.org/10.1016/j.progpolymsci.2004.04.001.

[27] A. Di Martino, M. Sittinger, M. V. Risbud, Chitosan: A versatile biopolymer for orthopaedic tissue-engineering, Biomaterials. (2005). https://doi.org/10.1016/j.biomaterials.2005.03.016.

[28] A. Arjunan, A. Baroutaji, J. Robinson, C. Wang, Antibacterial Biomaterials in Orthopedics, in: Ref. Modul. Mater. Sci. Mater. Eng., Elsevier, 2021. https://doi.org/https://doi.org/10.1016/B978-0-12-815732-9.00131-5.

[29] H.H. Lara, E.N. Garza-Treviño, L. Ixtepan-Turrent, D.K. Singh, Silver nanoparticles are broad-spectrum

bactericidal and virucidal compounds, J. Nanobiotechnology. 9 (2011) 2–9. https://doi.org/10.1186/1477-3155-9-30.

[30] Z. Sun, K. (Ken) Ostrikov, Future antiviral surfaces: Lessons from COVID-19 pandemic, Sustain. Mater. Technol. 25 (2020) e00203. https://doi.org/10.1016/j.susmat.2020.e00203.

[31] A. Arjunan, J. Robinson, E. Al Ani, W. Heaselgrave, A. Baroutaji, C. Wang, Mechanical performance of additively manufactured pure silver antibacterial bone scaffolds, J. Mech. Behav. Biomed. Mater. 112 (2020) 104090. https://doi.org/10.1016/j.jmbbm.2020.104090.

[32] S.S. Jeremiah, K. Miyakawa, T. Morita, Y. Yamaoka, A. Ryo, Potent antiviral effect of silver nanoparticles on SARS-CoV-2, Biochem. Biophys. Res. Commun. 533 (2020) 195–200. https://doi.org/10.1016/j.bbrc.2020.09.018.

[33] A. Arjunan, A. Baroutaji, A.S. Praveen, J. Robinson, C. Wang, Classification of Biomaterial Functionality, in: Ref. Modul. Mater. Sci. Mater. Eng., Elsevier, 2020. https://doi.org/https://doi.org/10.1016/B978-0-12-815732-9.00027-9.

[34] N. Hutasoit, B. Kennedy, S. Hamilton, A. Luttick, R.A. Rahman Rashid, S. Palanisamy, Sars-CoV-2 (COVID-19) inactivation capability of copper-coated touch surface fabricated by cold-spray technology, Manuf. Lett. 25 (2020) 93–97. https://doi.org/10.1016/j.mfglet.2020.08.007.

[35] V.A. Kokorekin, A. V. Gamayunova, V. V. Yanilkin, V.A. Petrosyan, Mediated electrochemical synthesis of copper nanoparticles in solution, Russ. Chem. Bull. 66 (2017) 2035–2043. https://doi.org/10.1007/s11172-017-1978-2.

[36] P. Makvandi, C. yu Wang, E.N. Zare, A. Borzacchiello, L. na Niu, F.R. Tay, Metal-Based Nanomaterials in Biomedical Applications: Antimicrobial Activity and Cytotoxicity Aspects, Adv. Funct. Mater. (2020). https://doi.org/10.1002/adfm.201910021.

[37] M.A. Syed, U. Manzoor, I. Shah, H.A. Bukhari, Antibacterial effects of Tungsten nanoparticles on the Escherichia coli strains isolated from catheterized urinary tract infection (UTI) cases and Staphylococcus aureus, New Microbiol. 33 (2010) 329–335.

[38] R.K. Matharu, L. Ciric, G. Ren, M. Edirisinghe, Comparative study of the antimicrobial effects of tungsten nanoparticles and tungsten nanocomposite fibres on hospital acquired bacterial and viral pathogens, Nanomaterials. 10 (2020). https://doi.org/10.3390/nano10061017.

[39] S. Raha, R. Mallick, S. Basak, A.K. Duttaroy, Is copper beneficial for COVID-19 patients?, Med. Hypotheses. 142 (2020) 109814. https://doi.org/10.1016/j.mehy.2020.109814.

[40] J. Robinson, M. Stanford, A. Arjunan, Stable Formation of Powder Bed Laser Fused 99.9% Silver, Mater. Today Commun. (2020) 101195. https://doi.org/10.1016/j.mtcomm.2020.101195.

[41] J. Robinson, M. Stanford, A. Arjunan, Correlation between selective laser melting parameters, pore defects and tensile properties of 99.9% silver, Mater. Today Commun. 25 (2020) 101550. https://doi.org/10.1016/j.mtcomm.2020.101550.

[42] J. Robinson, A. Arjunan, M. Stanford, I. Lyall, C. Williams, Effect of silver addition in copper-silver alloys fabricated by laser powder bed fusion in situ alloying, J. Alloys Compd. 857 (2021) 157561. https://doi.org/https://doi.org/10.1016/j.jallcom.2020.157561.

[43] A. Vance, K. Bari, A. Arjunan, Compressive performance of an arbitrary stiffness matched anatomical Ti64 implant manufactured using Direct Metal Laser Sintering, Mater. Des. 160 (2018) 1281–1294. https://doi.org/10.1016/j.matdes.2018.11.005.

[44] W. Phillips, N. Medcalf, K. Dalgarno, H. Makatsoris, S. Sharples, J. Srai, P. Hourd, D. Kapletia, Redistributed Manufacturing in Healthcare Creating New Value through Disruptive Innovation, n.d.

[45] W. Phillips, D. Kapletia, K. Dalgarno, P. Hunt, R. Bibb, H. Makatsoris, Q. Rafiq, S. Roscoe, B. Omar, N. Willoughby, A. Paterson, J. Benger, Innovation in healthcare manufacturing: transforming deployed

medical care, in: ISPIM Innov. Conf. - Innov. Our Common Futur., Loughborough University, Berlin, Germany, 2020. /articles/conference_contribution/Innovation_in_healthcare_manufacturing_transforming_deployed_medical_care/12571010/1 (accessed October 3, 2020).

[46] S. Li, U. Waheed, M. Bahshwan, L.Z. Wang, L.M. Kalossaka, J. Choi, F. Kundrak, A. Lattas, S. Ploumpis, S. Zafeiriou, C.W. Myant, A scalable mass customisation design process for 3D-printed respirator mask to combat COVID-19, Rapid Prototyp. J. ahead-of-print (2021). https://doi.org/10.1108/RPJ-10-2020-0231.

[47] A. Arjunan, M. Demetriou, A. Baroutaji, C. Wang, Mechanical performance of highly permeable laser melted Ti6Al4V bone scaffolds, J. Mech. Behav. Biomed. Mater. 102 (2020) 103517. https://doi.org/10.1016/j.jmbbm.2019.103517.

[48] J. Li, X. Cui, G.J. Hooper, K.S. Lim, T.B.F. Woodfield, Rational design, bio-functionalization and biological performance of hybrid additive manufactured titanium implants for orthopaedic applications: A review, J. Mech. Behav. Biomed. Mater. 105 (2020) 103671. https://doi.org/10.1016/j.jmbbm.2020.103671.

[49] S.N. Singh, V.S.S. Venkatesh, A.B. Deoghare, A review on the role of 3D printing in the fight against COVID-19: safety and challenges, Rapid Prototyp. J. 27 (2021) 407–420. https://doi.org/10.1108/RPJ-08-2020-0198.

[50] R. Moreno, D. Carou, D. Carazo-Álvarez, M.K. Gupta, Statistical models for the mechanical properties of 3D printed external medical aids, Rapid Prototyp. J. 27 (2021) 176–186. https://doi.org/10.1108/RPJ-02-2020-0033.

[51] R. Prabhu, J.S. Masia, J.T. Berthel, N.A. Meisel, T.W. Simpson, Maximizing design potential: investigating the effects of utilizing opportunistic and restrictive design for additive manufacturing in rapid response solutions, Rapid Prototyp. J. 27 (2021) 1161–1171. https://doi.org/10.1108/RPJ-11-2020-0297.

[52] P. Jeyachandran, S. Bontha, S. Bodhak, V.K. Balla, B. Kundu, M. Doddamani, Mechanical behaviour of additively manufactured bioactive glass/high density polyethylene composites, J. Mech. Behav. Biomed. Mater. 108 (2020) 103830. https://doi.org/https://doi.org/10.1016/j.jmbbm.2020.103830.

[53] M. Zanocco, F. Boschetto, W. Zhu, E. Marin, B.J. McEntire, B.S. Bal, T. Adachi, T. Yamamoto, N. Kanamura, E. Ohgitani, K. Yamamoto, O. Mazda, G. Pezzotti, 3D-additive deposition of an antibacterial and osteogenic silicon nitride coating on orthopaedic titanium substrate, J. Mech. Behav. Biomed. Mater. 103 (2020) 103557. https://doi.org/https://doi.org/10.1016/j.jmbbm.2019.103557.

[54] F. Calignano, Investigation of the accuracy and roughness in the laser powder bed fusion process, Virtual Phys. Prototyp. 13 (2018) 97–104. https://doi.org/10.1080/17452759.2018.1426368.

[55] M. Martí, A. Tuñón-Molina, F.L. Aachmann, Y. Muramoto, T. Noda, K. Takayama, Á. Serrano-Aroca, Protective Face Mask Filter Capable of Inactivating SARS-CoV-2, and Methicillin-Resistant Staphylococcus aureus and Staphylococcus epidermidis, Polym. 2021, Vol. 13, Page 207. 13 (2021) 207. https://doi.org/10.3390/POLYM13020207.

[56] D. Baltimore, Expression of animal virus genomes., Bacteriol. Rev. 35 (1971) 235–241. https://doi.org/10.1128/br.35.3.235-241.1971.

[57] M. Colopi, L. Caprio, A.G.G. Demir, B. Previtali, Selective laser melting of pure Cu with a 1 kW single mode fiber laser, 2018. https://www.sciencedirect.com/science/article/pii/S221282711830814X (accessed January 19, 2019).

[58] R. Guschlbauer, S. Momeni, F. Osmanlic, C. Körner, Process development of 99.95% pure copper processed via selective electron beam melting and its mechanical and physical properties, Mater. Charact. 143 (2018) 163–170. https://doi.org/10.1016/J.MATCHAR.2018.04.009.

[59] Z. Xiong, P. Zhang, C. Tan, D. Dong, W. Ma, K. Yu, Selective Laser Melting and Remelting of Pure Tungsten, Adv. Eng. Mater. 22 (2020) 1–9. https://doi.org/10.1002/adem.201901352.

[60] X. Zhou, X. Liu, D. Zhang, Z. Shen, W. Liu, Balling phenomena in selective laser melted tungsten, J. Mater. Process. Technol. 222 (2015) 33–42. https://doi.org/10.1016/j.jmatprotec.2015.02.032.

[61] T.Q. Tran, A. Chinnappan, J.K.Y. Lee, N.H. Loc, L.T. Tran, G. Wang, V.V. Kumar, W.A.D.M. Jayathilaka, D. Ji, M. Doddamani, S. Ramakrishna, 3D printing of highly pure copper, Metals (Basel). 9 (2019) 12–20. https://doi.org/10.3390/met9070756.

[62] C. Tan, K. Zhou, T. Kuang, Selective laser melting of tungsten-copper functionally graded material, Mater. Lett. 237 (2019) 328–331. https://doi.org/10.1016/j.matlet.2018.11.127.

[63] A.M. Vilardell, I. Yadroitsev, I. Yadroitsava, M. Albu, N. Takata, M. Kobashi, P. Krakhmalev, D. Kouprianoff, G. Kothleitner, A. du Plessis, Manufacturing and characterization of in-situ alloyed Ti6Al4V(ELI)-3 at.% Cu by laser powder bed fusion, Addit. Manuf. 36 (2020). https://doi.org/10.1016/j.addma.2020.101436.

[64] G. Carro, A. Muñoz, M.A. Monge, B. Savoini, A. Galatanu, M. Galatanu, R. Pareja, Thermal conductivity and diffusivity of Cu-Y alloys produced by different powder metallurgy routes, Fusion Eng. Des. 124 (2017) 1156–1160. https://doi.org/10.1016/j.fusengdes.2017.01.017.

[65] P. Bajaj, J. Wright, I. Todd, E.A. Jägle, Predictive process parameter selection for Selective Laser Melting Manufacturing: Applications to high thermal conductivity alloys, Addit. Manuf. 27 (2019) 246–258. https://doi.org/10.1016/j.addma.2018.12.003.

[66] M.K. Thompson, G. Moroni, T. Vaneker, G. Fadel, R.I. Campbell, I. Gibson, A. Bernard, J. Schulz, P. Graf, B. Ahuja, F. Martina, Design for Additive Manufacturing: Trends, opportunities, considerations, and constraints, CIRP Ann. - Manuf. Technol. 65 (2016) 737–760. https://doi.org/10.1016/j.cirp.2016.05.004.

[67] T.E. Johnson, A.T. Gaynor, Three-dimensional projection-based topology optimization for prescribed-angle self-supporting additively manufactured structures, Addit. Manuf. 24 (2018) 667–686. https://doi.org/10.1016/j.addma.2018.06.011.

[68] S.A.M. Tofail, E.P. Koumoulos, A. Bandyopadhyay, S. Bose, L. O'Donoghue, C. Charitidis, Additive manufacturing: scientific and technological challenges, market uptake and opportunities, Mater. Today. 21 (2018) 22–37. https://doi.org/10.1016/j.mattod.2017.07.001.

[69] H. Palza, M. Nuñez, R. Bastías, K. Delgado, In situ antimicrobial behavior of materials with copper-based additives in a hospital environment, Int. J. Antimicrob. Agents. 51 (2018) 912–917. https://doi.org/10.1016/j.ijantimicag.2018.02.007.

[70] M. Nicola, C. Sohrabi, G. Mathew, A. Kerwan, A. Al-Jabir, M. Griffin, M. Agha, R. Agha, Health policy and leadership models during the COVID-19 pandemic: A review, Int. J. Surg. 81 (2020) 122–129. https://doi.org/10.1016/j.ijsu.2020.07.026.

[71] T.L. Leirmo, O. Semeniuta, K. Martinsen, Tolerancing from STL data: A Legacy Challenge, Procedia CIRP. 92 (2020) 218–223. https://doi.org/10.1016/j.procir.2020.05.180.

[72] A. Manmadhachary, Y. Ravi Kumar, L. Krishnanand, Improve the accuracy, surface smoothing and material adaption in STL file for RP medical models, J. Manuf. Process. 21 (2016) 46–55. https://doi.org/10.1016/j.jmapro.2015.11.006.

[73] E. Huotilainen, R. Jaanimets, J. Valášek, P. Marcián, M. Salmi, J. Tuomi, A. Mäkitie, J. Wolff, Inaccuracies in additive manufactured medical skull models caused by the DICOM to STL conversion process, J. Cranio-Maxillofacial Surg. 42 (2014) 259–265. https://doi.org/10.1016/j.jcms.2013.10.001.

[74] P. O'Regan, P. Prickett, R. Setchi, G. Hankins, N. Jones, Metal Based Additive Layer Manufacturing: Variations, Correlations and Process Control, Procedia Comput. Sci. 96 (2016) 216–224. https://doi.org/10.1016/j.procs.2016.08.134.

[75] I. Yadroitsev, A. Gusarov, I. Yadroitsava, I. Smurov, Single track formation in selective laser melting of metal powders, J. Mater. Process. Technol. 210 (2010) 1624–1631.

https://doi.org/10.1016/j.jmatprotec.2010.05.010.

[76] A.A. Aversa, E. Librera, M. Hadi, G. Marchese, D. Manfredi, F. Calignano, S. Biamino, M. Pavese, PT SC, J. Mater. Process. Tech. (2017). https://doi.org/10.1016/j.jmatprotec.2017.11.055.

[77] A. Iveković, N. Omidvari, B. Vrancken, K. Lietaert, L. Thijs, K. Vanmeensel, J. Vleugels, J.P. Kruth, Selective laser melting of tungsten and tungsten alloys, Int. J. Refract. Met. Hard Mater. 72 (2018) 27–32. https://doi.org/10.1016/j.ijrmhm.2017.12.005.

[78] P. Charalampous, I. Kostavelis, D. Tzovaras, Non-destructive quality control methods in additive manufacturing: a survey, Rapid Prototyp. J. 26 (2020) 777–790. https://doi.org/10.1108/RPJ-08-2019-0224.

[79] J. Fieres, P. Schumann, C. Reinhart, Predicting failure in additively manufactured parts using X-ray computed tomography and simulation, Procedia Eng. 213 (2018) 69–78. https://doi.org/10.1016/j.proeng.2018.02.008.

[80] N. Ortega, S. Martínez, I. Cerrillo, A. Lamikiz, E. Ukar, Computed tomography approach to quality control of the Inconel 718 components obtained by additive manufacturing (SLM), Procedia Manuf. 13 (2017) 116–123. https://doi.org/10.1016/j.promfg.2017.09.018.

[81] H. Nikkhah, A. Baroutaji, Z. Kazancı, A. Arjunan, Evaluation of crushing and energy absorption characteristics of bio-inspired nested structures, Thin-Walled Struct. 148 (2020) 106615. https://doi.org/10.1016/j.tws.2020.106615.

[82] A. Arjunan, M. Singh, A. Baroutaji, C. Wang, Additively manufactured AlSi10Mg inherently stable thin and thick-walled lattice with negative Poisson's ratio, Compos. Struct. 247 (2020) 112469. https://doi.org/10.1016/j.compstruct.2020.112469.

[83] F. Najarian, R. Alipour, M. Shokri Rad, A.F. Nejad, A. Razavykia, Multi-objective optimization of converting process of auxetic foam using three different statistical methods, Measurement. 119 (2018) 108–116. https://doi.org/10.1016/J.MEASUREMENT.2018.01.064.

[84] A.S. Praveen, A. Arjunan, Parametric optimisation of High-Velocity Oxy-Fuel Nickel-Chromium-Silicon-Boron and Aluminium-Oxide coating to improve erosion wear resistance, Mater. Res. Express. (2019). https://doi.org/10.1088/2053-1591/ab301c.

[85] A.S. Praveen, A. Arjunan, Effect of nano-Al<inf>2</inf>O<inf>3</inf> addition on the microstructure and erosion wear of HVOF sprayed NiCrSiB coatings, Mater. Res. Express. 7 (2019). https://doi.org/10.1088/2053-1591/ab5bda.

[86] R.H. Myers, D.C. Montgomery, C.M. Anderson-Cook, Response Surface Methodology: Process and Product Optimization Using Designed Experiments, Wiley, 2011. https://books.google.co.uk/books?id=F6MJeRe2POUC.

[87] S. Jakhmola, O. Indari, D. Kashyap, N. Varshney, A. Rani, C. Sonkar, B. Baral, S. Chatterjee, A. Das, R. Kumar, H.C. Jha, Recent updates on COVID-19: A holistic review, Heliyon. 6 (2020) e05706. https://doi.org/10.1016/j.heliyon.2020.e05706.

[88] K.M. Perkins, N. Munguia, M. Ellenbecker, R. Moure-Eraso, L. Velazquez, COVID-19 pandemic lessons to facilitate future engagement in the global climate crisis, J. Clean. Prod. (2020) 125178. https://doi.org/10.1016/j.jclepro.2020.125178.

[89] V.A. Ryabkova, L.P. Churilov, Y. Shoenfeld, Influenza infection , SARS , MERS and COVID-19 : Cytokine storm – The common denominator and the lessons to be learned, Clin. Immunol. 223 (2021) 108652. https://doi.org/10.1016/j.clim.2020.108652.

[90] M. Mofijur, I.M.R. Fattah, M.A. Alam, A.B.M.S. Islam, H.C. Ong, S.M.A. Rahman, G. Najafi, S.F. Ahmed, M.A. Uddin, T.M.I. Mahlia, Impact of COVID-19 on the social, economic, environmental and energy domains: Lessons learnt from a global pandemic, Sustain. Prod. Consum. 26 (2021) 343–359. https://doi.org/10.1016/j.spc.2020.10.016.

[91] T.D. Ngo, A. Kashani, G. Imbalzano, K.T.Q. Nguyen, D. Hui, Additive manufacturing (3D printing): A review of materials, methods, applications and challenges, Compos. Part B Eng. 143 (2018) 172–196. https://doi.org/10.1016/j.compositesb.2018.02.012.

[92] A. Arjunan, A. Baroutaji, J. Robinson, A.S. Praveen, A. Pollard, C. Wang, Future Directions and Requirements for Tissue Engineering Biomaterials, in: Ref. Modul. Mater. Sci. Mater. Eng., Elsevier, 2021. https://doi.org/https://doi.org/10.1016/B978-0-12-815732-9.00068-1.

[93] A. Arjunan, A. Baroutaji, J. Robinson, C. Wang, Tissue Engineering Concept, in: Ref. Modul. Mater. Sci. Mater. Eng., Elsevier, 2021. https://doi.org/https://doi.org/10.1016/B978-0-12-815732-9.00120-0.

[94] M. Di Prima, J. Coburn, D. Hwang, J. Kelly, A. Khairuzzaman, L. Ricles, Additively manufactured medical products – the FDA perspective, 3D Print. Med. 2 (2016) 1. https://doi.org/10.1186/s41205-016-0005-9.

[95] E. Cuesta, B.J. Alvarez, P. Zapico, S. Giganto, Analysis of post-processing influence on the geometrical and dimensional accuracy of selective laser melting parts, Rapid Prototyp. J. 26 (2020) 1713–1722. https://doi.org/10.1108/RPJ-02-2020-0042.